Streak Instabilities on HIFiRE-5 Elliptic Cone

Meelan Choudhari,* Fei Li†
NASA Langley Research Center, Hampton, VA, 23681

Pedro Paredes‡
National Institute of Aerospace, Hampton, VA, 23666

The Hypersonic International Flight Research and Experimentation (HIFiRE) 5 flight experiment by the Air Force Research Laboratories and Australian Defense Science and Technology Organization yielded in-flight, hypersonic transition data for a canonical, 3D configuration in the form of an elliptic cone at various combinations of angle-of-attack and yaw. Previous analysis has shown that boundary-layer stability calculations for the as-flown, zero-yaw flight conditions are able to capture the second mode dominated transition along the attachment line as well as the crossflow induced transition in between the attachment line and the minor axis symmetry plane. However, there is still a need to understand the transition in the vicinity of the minor axis plane of symmetry, where the boundary layer thickness exhibits an azimuthally compact bulge due to the collision of the secondary flow approaching from the attachment lines on both sides. This paper reports a computational analysis of the stability of the boundary layer flow along the bulge regions on both the leeward and windward sides of the vehicle surface. At a representative flight condition corresponding to a time instant of t = 514.813 seconds, computations are performed to identify several different unstable modes within the bulge regions, with the eventual goal of developing a linear stability correlation for the transition onset near the minor axis symmetry plane. The most amplified flow instabilities in the pretransitional region correspond to a "stem" mode that is concentrated within a pair of nearly vertical shear layers below the cap of the mushroom shaped bulge in the mean velocity contours. An excellent agreement is found between the predictions of instability amplification based on the plane marching parabolized stability equations (PSE) and the direct numerical solutions (DNS). Given the large number of unstable modes within the bulge region, the observed agreement demonstrates, for first time, that the PSE can provide accurate predictions for the development of flow instabilities in streak-like flow features over three-dimensional bodies. The peak N-factor of approximately 15 at the transition location estimated from the thermocouple measurements along the leeward centerline is close to the transition N-factor for Mack mode transition during the HIFiRE-1 circular cone flight experiment with nearly zero degrees angle of attack.

Nomenclature

f = frequency of instability waves [kHz]
M_∞ = freestream Mach number (nondimensional)
M_e = Mach number at the edge of the boundary layer (nondimensional)
N = logarithmic amplification ratio of a fixed frequency secondary instability mode (nondimensional)
p' = pressure fluctuation [Pa]
P_∞ = freestream pressure [Pa]
Re = freestream unit Reynolds number [m^{-1}]
t = time [sec]
T_0 = stagnation temperature [K]
T_{ad} = adiabatic wall temperature [K]
T_w = wall temperature [K]
T_∞ = freestream temperature [K]
u = streamwise velocity [m/s]
u' = fluctuation in streamwise velocity [m/s]

* Aerospace Technologist, Meelan.M.Choudhari@nasa.gov, Fellow, AIAA.
† Aerospace Technologist, Fei.Li@nasa.gov
‡ Research Engineer, pedro.paredesgonzalez@nasa.gov, Senior Member, AIAA.

U_∞ = freestream velocity [m/s]
X = axial distance [m]
Y = wall-normal distance [m]
Z = azimuthal distance from symmetry plane [m]
α = angle of attack [deg]
β = yaw angle [deg]
η = surface normal distance [m]
ρ = fluid density [kg/m^3]
θ = azimuthal coordinate with respect to windward meridian [rad]

I. Introduction

Boundary layer transition from the laminar to a turbulent state is known to have a major impact on the design and performance of hypersonic flight vehicles. When the vehicle surface is relatively smooth, the transition process is initiated by linear instabilities of the laminar boundary layer, including second (or Mack) mode instability, Görtler instabilities, stationary and traveling modes of crossflow instability, and the attachment-line instability. Regardless of the speed regime, linear stability correlations have been quite successful in predicting the onset of transition when a single instability mechanism dominates the transition process. Mixed mode transition has been more challenging to predict because of the potentially stronger influence of nonlinear interactions between the relevant modes of instability.

The simplest canonical configurations that include the necessary elements for studying transition due to multiple instability mechanisms in a hypersonic boundary-layer flow correspond to a circular cone at small but nonzero angle of attack [1–8] and an elliptic cone [9–16]. As discussed in these references, much of the earlier data for the two canonical configurations was obtained in conventional (i.e., noisy) ground facilities, but quiet tunnel measurements have also become increasingly common over the past decade. In-flight transition data for these two configurations has been obtained during the Hypersonic International Flight Research Experimentation (HIFiRE) program conducted jointly by the Air Force Research Laboratory (AFRL) and the Australian Defence Science and Technology Organization (DSTO) [17]. Two HIFiRE flights were devoted to boundary layer transition measurements. The primary experiment on HIFiRE-1 was devoted to second-mode transition on a circular cone at zero degrees angle of attack [18–19], but the descent phase of the flight actually yielded transition measurements at significantly large angles of attack [20]. The HIFiRE-5b transition experiment extended the HIFiRE-1 data to include a fully three-dimensional, hypersonic configuration in the form of a nonablating, 2:1 elliptic cone [21–23].

As revealed in the preflight transition analysis of the HIFiRE-5 configuration [12, 16, 24], the elliptic cone model can support a variety of instabilities that dominate in different portions of the model surface, including attachment line instabilities, second mode waves, stationary and traveling crossflow instabilities, and more complex, localized instabilities in the bulge region associated with the collision of the secondary flow approaching from both attachment lines. The various publications related to the HIFiRE-5 program [25–50] include both the flight experiments and various ground facility measurements of instability and/or transition over the elliptic cone under a variety of disturbance environments representing both conventional and quiet facilities. Such multipronged investigations have provided valuable insights into the effects of the disturbance environment on the amplification of the various types of instability waves over the HIFiRE-5 configuration. For example, quiet tunnel measurements of traveling crossflow instability on an elliptic cone [33] have yielded encouraging comparisons with the linear stability predictions [51].

Post flight transition analysis for selected trajectory locations during the HIFiRE-5b flight experiment has been reported by Tufts et al. [52] and Moyes et al. [53]. The work by Tufts et al. [52] has shown that linear stability calculations yield a satisfactory correlation with second mode dominated transition along the attachment line as well as crossflow induced transition in between the attachment lines and the narrow regions of boundary layer bulge associated with the collision of the secondary flow approaching from the attachment lines. However, the transition mechanisms within the bulge region have not been examined as yet. Preflight analysis [12, 16, 24] had shown that the instabilities within the bulge region cannot be predicted via conventional stability analysis because of the strongly inhomogeneous nature of the boundary layer flow in that region. Specifically, the azimuthal variations in the basic state can become comparable to the wall-normal gradients, requiring multidimensional, i.e., partial-differential-equation (PDE) based instability analysis techniques to predict the amplification of the various unstable modes supported by the bulge region [12]. At the zero-yaw condition analyzed by Tufts et al. [52], the bulge region

is centered on the symmetry plane of the boundary layer flow. The objective of this ongoing research is to examine the instability characteristics of the bulge region at the above condition and to assess the prospects for using N-facor methods to estimate the onset of transition. A similar analysis for axisymmetric bodies at nonzero incidence in the supersonic Mach number regime was described in Refs. [54, 55].

The instability evolution over the bulge region bears considerable similarities with the previous work at the NASA Langley Research Center on the secondary instability of stationary crossflow vortices in the hypersonic boundary layer flow over a yawed circular cone [56–59] and of the Görtler vortices over a concave cone configuration [60, 61]. The secondary instability of azimuthally (locally) periodic crossflow vortices was investigated in Refs. [56, 57], whereas the instabilities of an azimuthally compact crossflow vortex pattern were examined in Refs. [58, 59]. These studies have shown that the instabilities of azimuthally modulated hypersonic boundary layers can be divided into two main classes. The first class of disturbances involves azimuthally modulated counterparts of the Mack mode instability in boundary layer flows that are quasihomogeneous in the azimuthal direction, and therefore, these modes can extend beyond the region of the short-scale azimuthal variation in the underlying basic state. The other class of instabilities is intrinsically linked with the azimuthal inhomogeneity of the basic state and these modes tend to concentrate inside one or more localized regions of high shear that characterize the crossplane variation in the basic state. Given the physical similarities between the bulge region over the HIFiRE-5b vehicle and the basic states examined in the aforementioned works, the present work follows a similar computational strategy as the earlier studies from Refs. [56–59, 62, 63], in that all of these studies include a synergistic application of multifidelity models ranging from a local, multidimensional instability analysis, the plane marching parabolized stability equations, and direct numerical simulations. The local eigenvalue analysis provides the initial conditions for the PSE marching, which in turn can be validated against the DNS. In that regard, the present paper advances the previous computations from an underlying axisymmetric cone or flat plate geometry to the fully 3D shape of an elliptic cone.

The remaining sections of this paper are laid out as follows. A brief summary of the flow configuration of interest is given in Section II, which also describes the basic state boundary layer flow over the HIFiRE-5b configuration at the selected instant during flight. The analysis of linear instabilities sustained by the bulge region is described in Section III. Conclusions are outlined in Section IV.

II. Flow Configuration and the Basic State

The HIFiRE-5b test article consists of a blunt-nosed elliptic cone of 2:1 ellipticity, 0.86 meters in length. The minor axis of the cone is a seven-degree half-angle. The nose tip cross-section in the minor axis describes a 2.5 mm radius circular arc, tangent to the cone ray describing the minor axis, and retains a 2:1 elliptical cross-section to the tip. Therefore, the model contour along any given meridian involves a curvature discontinuity at the juncture between the nose and the downstream cone portion. The cone is 431.8 mm wide at its base and overhangs the 355.6 mm diameter booster in the yaw plane. An uninstrumented section blends the elliptical cone cross-section into the circular booster cross section. The vehicle is spin-stabilized. Cant-angle on the first and second-stage fins causes the vehicle to spin passively. Because of this, the payload rolls at a very slow rate throughout the ascent and descent.

The flow condition of interest corresponds to that targeted in the analysis by Tufts et al. [52], which modeled the flight conditions at $t = 514.83$ seconds, namely, a freestream Mach number of $M_\infty = 7.8$, freestream velocity, pressure, and temperature corresponding to $U_\infty = 2295.9$ m/s, $P_\infty = 3435$ Pa, and $T_\infty = 215.6$ K, respectively, a unit Reynolds number equal to $Re = 9.0\times10^6$/m, and an approximate surface temperature of $T_w = 373.15$ K (i.e., $T_w/T_0 = 0.131$). Whereas the computations reported by Tufts et al. were performed for $\alpha = -1.0$ degrees, we use the best estimate for the angle of attack at $t = 514.83$ seconds, corresponding to $\alpha = -1.2$ degrees.

To provide a basic state for the prediction of the disturbance amplification characteristics, mean flow computations were carried out using the VULCAN (Viscous Upwind aLgorithm for Complex flow ANalysis) software [64]. The code solves the unsteady, conservation equations appropriate for laminar or turbulent flow of calorically or thermally perfect gases with a spatially second-order accurate cell-centered finite volume scheme. In the present computations, the inviscid fluxes were constructed using the MUSCL $\kappa = 0$ scheme, the van Albada gradient limiter [65] and the Low Dissipation Flux Split Scheme (LDFSS) of Edwards [66-67]. The cell face gradients required to construct the viscous fluxes were obtained using an auxiliary control volume approach that results in a compact viscous stencil that produces a second-order accurate approximation of the full Navier-Stokes viscous fluxes. Throughout the computations, special care was exercised to ensure an appropriate resolution of the boundary layer flow while maintaining a close alignment of the outer grid with the 3D shock surface. The computed

basic state was fully laminar with the assumption of ideal gas behavior; no turbulence model or real-gas approximations were included in these computations.

In previous unpublished work, similar computations of the mean flow over a 0.381 scale wind tunnel configuration were cross-validated against the solutions obtained with the LAURA code [68] for various grid sizes. Additional grid convergence analysis for that same flow configuration was reported by Li et al. [51].

For the baseline vehicle attitude corresponding to zero yaw angle, $\beta = 0$ degrees, the computational domain included just one half of the total body surface. The grid topology was effectively equivalent to a structured grid consisting of two blocks, one near the nose and a second one that covered most of the body length downstream of the nose. The downstream block was discretized using 1201 points in the axial (X) direction, 1441 points in the azimuthal (θ) direction, and 513 points in the surface normal (η) direction. The grid was nonsingular within the nose region and was suitably clustered in all three computational coordinates. For grid convergence studies, additional computations were done by using smaller numbers of points along both surface coordinates as well as by varying the degree of grid clustering within the bulge region and the azimuthal region beyond the bulge. The boundary conditions employed during the mean flow computations were typical of blunt body computations involving symmetry conditions along the azimuthal boundaries. Mach number contours at selected stations along the cone length are shown in Fig. 1. The Mach number contours clearly indicate the emergence of the bulge region near the symmetry planes on the leeward as well as the windward sides. A comparison of the axial velocity contours obtained with two different grids is shown in Fig. 2. For the bulge region of interest, a satisfactory grid convergence is observed at all axial locations (see, for example, Figs. 2(a) and 2(b) for basic state contours across the length of the cone). The computed mode shapes of instability waves in Refs. [12, 16, 24] indicate that the peak fluctuations associated with those waves are often confined to the high shear regions within the bulge. On the basis of the agreement between the solutions presented in Fig. 2, one may infer that the relevant high-shear regions are adequately captured within the present computation of the basic state.

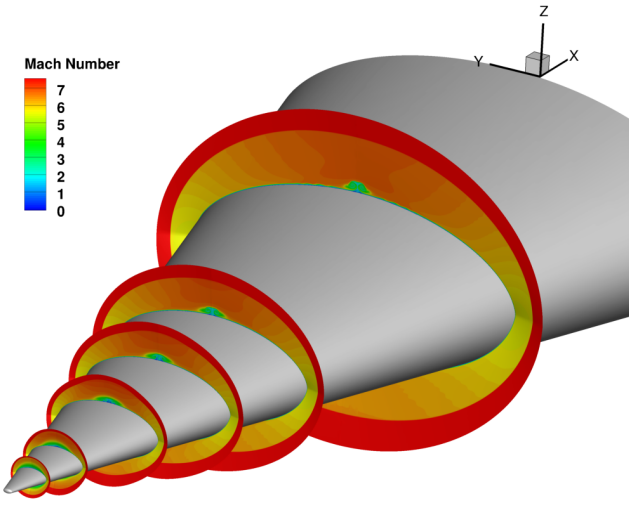

Fig. 1. Mach number contours of the basic state at t = 514.83 seconds, indicating the bulge region along the minor axis plane of symmetry (Y = 0 m). Crossplane contours are shown at axial locations of $X \approx$ 0.05, 0.1, 0.2, 0.3, 0.4, and 0.7 meters, respectively.

A comparison between the Mach number contours from Figs. 2(a) and 2(b) also indicates how the benign bulge in boundary layer thickness at X = 0.2 m develops a different structure downstream as a result of the continued evolution of the secondary flow. The crossplane contours at X = 0.2 m reveal two pairs of regions indicating a roll-up of the near wall fluid (see, for instance, the low-speed regions indicated in blue within Fig. 3(a)), caused by an upwelling of the secondary flow within the crossplane. The crossplane distributions of streamwise vorticity (not shown here) indicate a strong pair of vortex structures on the side of the cap region of the mushroom shaped contours, along with additional pairs that are closer to the surface in the vicinity of the blue shaded structures. At X > 0.2 m, the smaller structures near the outer pair of blue colored regions in Fig. 3(a) get pushed toward the

symmetry plane as a result of the velocity induced by the larger vortex structures within the sides of the mushroom cap. Eventually, the two regions of low-speed flow merge with each other, yielding a single pair of shear layers comprising the stem of the mushroom shaped contours at X = 0.7 m (Fig. 2(b)). For future reference, Table 1 summarizes the bulge region characteristics at selected axial stations.

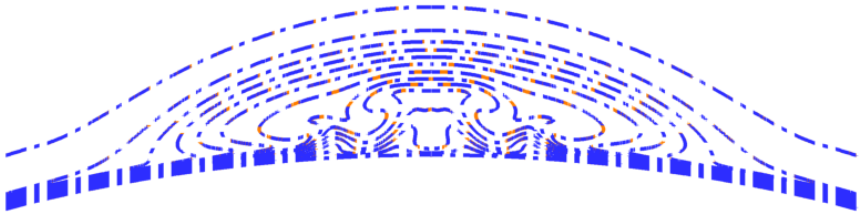

(a) X = 0.2 m.

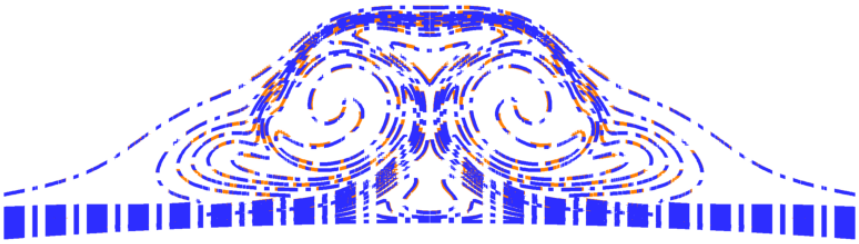

(b) X = 0.7 m.

Fig. 2. Mach number contours of the basic state near the bulge region centered on Y = 0 (corresponding to vertical plane of symmetry) on the leeward side. Contour values range from 0 to 7.5, in increments of 0.5. Results are shown for the baseline grid (blue lines) and a coarser grid with half the number of points in each surface direction (orange lines).

Figure 3(b) depicts the crossplane contours of $\rho|\nabla_{YZ}(u)|$ where ∇_{YZ} denotes the crossplane gradient within the Y-Z plane. The regions of high shear correspond to the near wall flow, including two pairs of lift up from the wall as seen in Fig. 3(a) and a nearly horizontal shear layer that is associated with the cap of the mushroom structure.

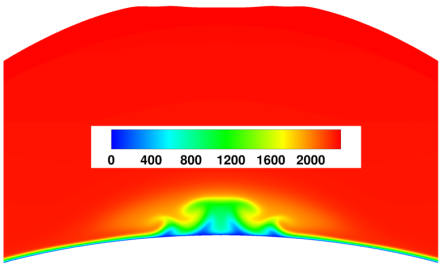

(a) Axial velocity (u) contours

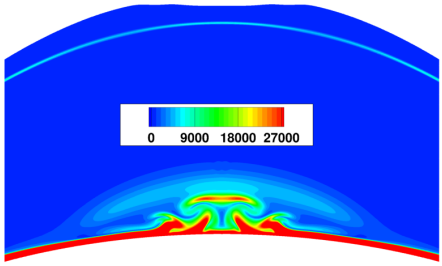

(b) Contours of $\rho|\nabla_{YZ}(u)|$, i.e., the magnitude of density weighted crossplane gradient of u

Fig. 3. Axial velocity contours of the basic state near the bulge region on the leeward side (X = 0.2 m).

Table 1 Boundary layer characteristics along the leeward and windward planes of symmetry

X (m)	M_e (leeward)	T_w/T_{ad} (leeward)	M_e (windward)	T_w/T_{ad} (windward)
0.1	3.70	0.15	3.59	0.15
0.2	5.59	0.15	5.38	0.15
0.3	6.57	0.15	6.21	0.15
0.4	6.72	0.15	6.34	0.15
0.5	6.75	0.15	6.37	0.15

As previously discussed in the context of the basic state computations for a 0.381:1 scale wind tunnel configuration [51], the flowfield in the vicinity of the symmetry plane is sensitive to the details of the computational process and a rigorous demonstration of the insensitivity of the computed basic state to those details can be a challenging goal in practice. To build further confidence into the numerical results, basic state computations were also carried out with a higher-order flow solver and a computational mesh that was obtained by keeping every other wall-normal point from the finer mesh in Fig. (2) and approximately every third grid point in the axial direction. A detailed description of the governing equations and their numerical discretization used in this solver is given by Wu et al. [69]. The inviscid fluxes from the governing equations are computed by using a seventh-order weighted essentially nonoscillatory (WENO) finite-difference scheme introduced by Jiang and Shu [70]; but the solver also allows the use of limiters [69, 71] that have been optimized to reduce the numerical dissipation. Both an absolute limiter on the WENO smoothness measurement and a relative limiter on the total variation are employed simultaneously during the simulation. The viscous fluxes are discretized using a fourth-order central difference scheme and time integration is performed using a third-order low-storage Runge-Kutta scheme [72]. In previous studies, this numerical code has been applied to the simulation of hypersonic turbulent boundary layers [73] as well as the laminar-turbulent transition due to crossflow instability in swept wing boundary layers [74, 75]. The lessons learned from these simulations were applied to develop the computational grids for the DNS computations described in the present paper. The higher-order solution was limited to the region downstream of the nose. The comparison of Mach number contours based on the VULCAN solution and the DNS-WENO solution shows that the basic state contours based on the 6^{th}-order accurate solution are nearly identical to those obtained from the 2^{nd}-order solutions obtained with the VULCAN solver.

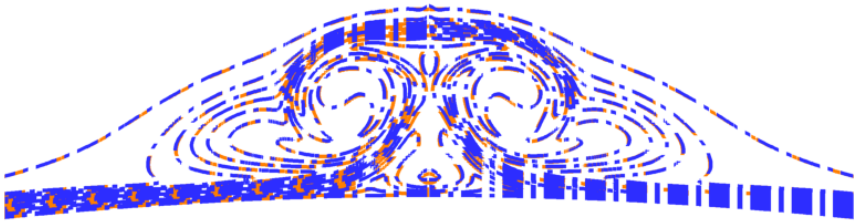

Fig. 4. Comparison of VULCAN (orange lines) and DNS-WENO (blue lines) solutions for the Mach number contours of the basic state near the bulge region (X = 0.5 m).

III. Linear Stability of the Flow within the Bulge Region

Analysis of the flight data at t = 514.83 seconds indicates that the onset of transition in the vicinity of the vehicle centerline was approximately midway along the length of the cone [48]. Therefore, the instability characteristics over the front portion of the cone are of greater interest for understanding the transition behavior at this particular time. As mentioned in the Introduction, the analysis of instability modes within the bulge region must account for the enhanced azimuthal gradients associated with the bulge. Because of the azimuthal symmetry of the basic state for the zero yaw condition of interest, the disturbances within the bulge region can be divided into symmetric (even) and antisymmetric (odd) modes on the basis of the azimuthal distribution of the axial velocity perturbation u'. Thus, the antisymmetric modes are associated with zero u' fluctuations (as well as zero fluctuations in the surface normal velocity and in all thermodynamic variables) at the symmetry plane (Y = 0), whereas the symmetric modes have zero azimuthal gradient in those quantities along Y = 0. To gain a basic understanding of these unstable modes, we first consider the instability characteristics based on local eigenvalue solutions at selected axial stations. Analogous to the secondary instability analysis of crossflow vortex modes on a yawed cone [56–59], the local instability analysis is performed in two different ways, namely, by invoking the quasiparallel approximation for the basic state and by retaining the axial gradients of the basic state. The latter option is denoted herein as a partially nonparallel (PNP) eigenvalue analysis.

Similar to the multidimensional stability analysis at the preflight conditions [12, 16, 24], a number of unstable modes are found at the flight condition of interest. The growth rate spectra for selected unstable modes obtained via the PNP eigenvalue analysis at X = 0.1 m are shown in Fig. 5(a), whereas Fig. 5(b) outlines the frequency dependence of the corresponding phase speeds. Analogous results for X = 0.2 m are shown in Fig. 6. Representative mode shapes for the selected mode types are included in Figs. 5(a) and 6(a), respectively. These results are obtained by using a crossplane of 201 points in the wall-normal direction and 151 points in the azimuthal

direction, along with sixth-order finite differences in the azimuthal and wall-normal directions, respectively. Sponge zones are used in both wall-normal and spanwise directions in order to enable sufficient decay of the disturbance amplitudes ahead of the outer boundaries. Additional computations were performed to ensure that the computed eigenvalues are insensitive to the computational grid and the sponge zones employed during these calculations. As discussed in Ref. [76] in the context of wake instabilities behind an isolated roughness element, a planar eigenvalue analysis in azimuthally inhomogeneous hypersonic boundary layers can reveal two types of unstable modes based on the azimuthal distribution of their fluctuations, namely, modes that are concentrated within the localized azimuthal inhomogeneity of the basic state (such as the bulge region) and modes that extend beyond the azimuthal inhomogeneity, well into the surrounding region of weaker azimuthal gradients and that may or may not have a noticeable signature within the region of the localized inhomogeneity. For the computations reported herein, the azimuthal domain is truncated within a finite distance from the bulge region, to help capture only those instability modes that are localized within the bulge region. Even when a subset of unstable modes associated with the Mack mode and crossflow instabilities within the surrounding region are captured within the eigenvalue computation, those modes are excluded from the results shown in this paper.

As discussed in the introduction (as well as in Refs. [56-59]), the instability modes within the bulge region can be further divided into two different subtypes on the basis of their wall-normal distribution. Both of these modal subtypes are observed collectively between the results shown in Figs. 5(a) and 6(a). The benign structure of the basic state at X = 0.1 m is characterized by a thickening of the boundary layer near the minor-axis plane of symmetry. This bulge region exhibits an internal shear layer near the top of the velocity contours (similar to that at X = 0.2 m in Fig. 3(b)) that is dominated by the azimuthal vorticity component. In comparison, the azimuthal variation of the basic state, or equivalently, its wall-normal vorticity is rather weak at this station. Thus, one expects that the Mack mode instability (suitably modulated by the moderate azimuthal variations in the boundary layer thickness) would play a significant role among the unstable modes at this station. Indeed, the group of three high-frequency modes in Fig. 5(a) denote the counterparts of the conventional second mode (i.e., Mack mode) waves and they have dual peaks in velocity fluctuations along the wall-normal direction. The symmetric mode IV(S) corresponds to the analog of an axisymmetric Mack mode whereas the mode V(A) corresponds to an oblique Mack mode with an azimuthal scale (or "wavelength") that is comparable to the spanwise extent of the shear layer. The mode VI(S) is a symmetric mode with an azimuthal scale that is approximately one half of the width of the shear layer. The phase speeds of all three mode families fall within a similar range is indicated in Fig. 5(b). Because the amplification rates of the Mack mode disturbances decrease quickly with a decreasing azimuthal wavelength (i.e., an increasing wave angle), the nearly planar mode IV(S) has the highest peak amplification rate among these three modes (and, in fact, among all unstable modes at this location). The peak amplification rate of mode V(A) is less than one half of the peak corresponding to the planar mode and the amplification rates of modes from the VI(S) family are uniformly small. All modes with azimuthal length scales that are shorter in comparison with that of the mode VI(S) are associated with decaying disturbances at this location. Finally, we note that the range of frequencies associated with the above group of modes increases slightly as the modes become increasingly oblique.

The mode shapes associated with the low frequency modes (i.e., modes I(S), II(A), and III(S)) indicate a somewhat (but not precisely) analogous progression in the azimuthal variation as the Mack mode group discussed above. However, the growth rates associated with all low-frequency modes are rather small, i.e., even smaller than the peak growth rate of the oblique Mack modes corresponding to the mode family VI(S), and furthermore, the variation of the peak amplification rate with the associated frequency is not monotonic in this case. Indeed, it is the mode III(s) that has the higher peak amplication rate within the group of low frequency modes. The most important distinction between the groups of low-frequency and high-frequency disturbances, respectively, corresponds to the wall-normal distribution of the respective fluctuations. Whereas all Mack modes induce significant fluctuations in the near wall region, the fluctuations associated with the lower frequency modes are always localized within the shear layer region that is located higher up within the bulge region. It is also noteworthy that the phase speeds of these shear-layer modes are actually confined to a significantly narrower range than that of the Mack modes.

As the azimuthal variations across the bulge region become stronger from X = 0.1 m to X = 0.2 m, the topology of the unstable modes changes significantly as seen in Fig. 6(a). First, and most important, the frequency bandwidth of most of the unstable modes at X = 0.2 m is significantly higher and there is also a significant overlap in frequency range across a majority of the unstable modes, with the exception of the modes V(S) and V(A) that are unstable within a rather narrow range of frequencies and correspond to supersonic phase speeds with respect to the local freestream as inferred from Fig. 6(b) and Table 1. Note that the two pairs of modes designated as V and VI are concentrated sufficiently farther from the symmetry plane so that the symmetry condition imposed on the eigenvalue problem has little influence on the amplification rates or the mode shapes of $|u'|$. Thus, the mode pairs

corresponding to symmetric and antisymmetric disturbances, respectively, within each mode number are essentially the same, with the exception of the relative phase angles between the *u'* fluctuations on either side of the plane of symmetry. It may also be noted that, unlike in Fig. 5(a), the peak growth rates of all six mode families plotted in Fig. 6(a) are comparable to each other. Finally, none of the modes at $X = 0.2$ m display the dual peak structure seen in Fig. 5(a), and with the exception of modes V(S) and V(A), the peak velocity fluctuations associated with the unstable modes at $X = 0.2$ m occur within the shear layers that are located away from the surface. Whereas modes I through IV reside in the primary shear layer within the cap region of the flattened mushroom structure, modes V and VI are concentrated within the region of secondary rollup that was discussed earlier with Figs. 2 and 3. The lower phase velocity of modes V (i.e., supersonic with respect to the local inviscid flow above the bulge region) is associated with the near-wall peak, where the base flow velocities are relatively lower. Although not shown in this paper, at $X \geq 0.3$ m, the number of unstable modes becomes even larger and the local amplification rates of some of those modes is higher than those in Figs. 5(a) and 6(a).

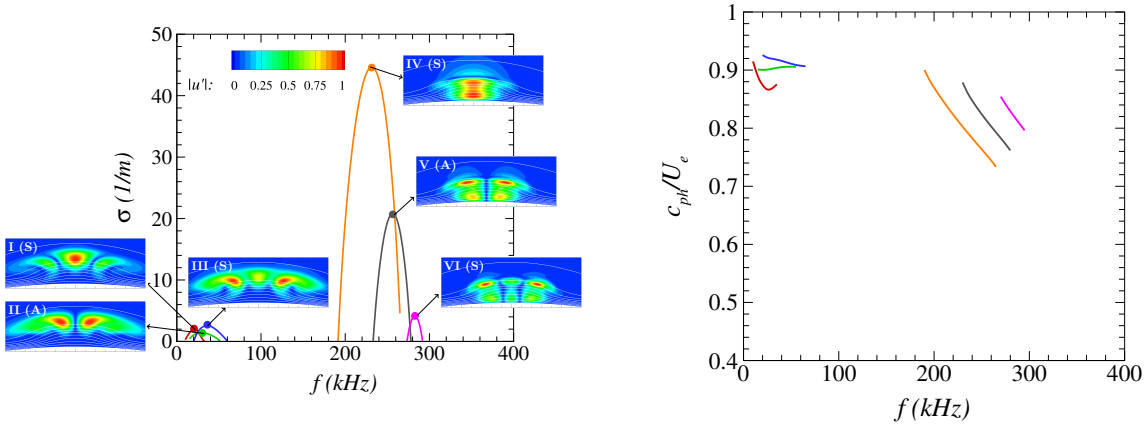

(a) *Growth rate spectra* (b) *Phase speed spectra*

Fig. 5. Growth rate and phase speed as functions of frequency for the relevant instability modes at $X = 0.10$ m. In general, the modes are numbered in the order of increasing frequency at the peak amplification rate and the label inside the parentheses next to the mode number indicates whether the mode corresponds to a symmetric or an antisymmetric mode. The representative mode shapes for each family (corresponding to the disturbance frequency indicated by the arrow) correspond to |*u'*|.

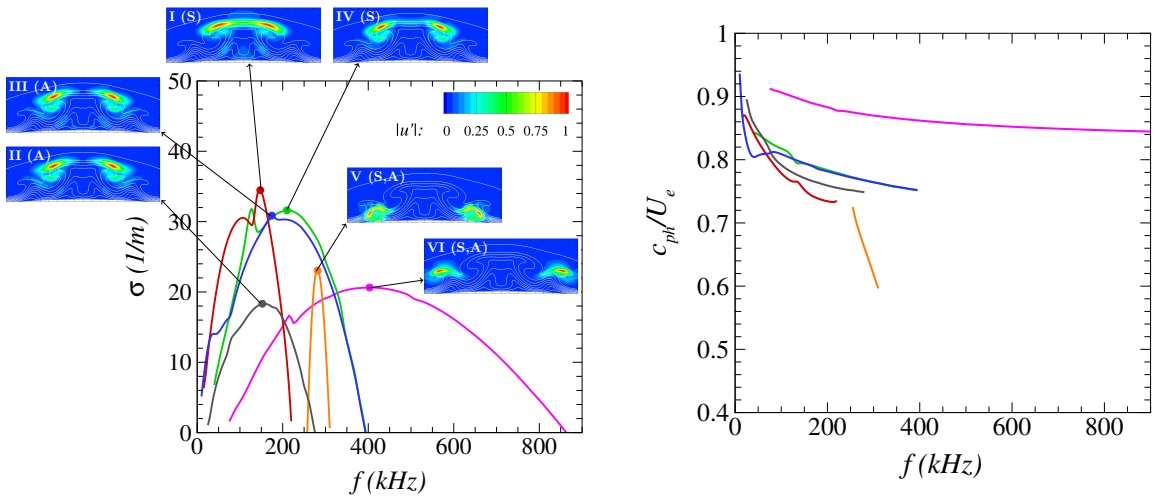

(a) *Growth rate spectra* (b) *Phase speed spectra*

Fig. 6. Growth rate and phase speed spectra for the relevant instability modes at $X = 0.20$ m.

To characterize the axial evolution of the unstable disturbances along the length of the cone, and thereby, establish a topological connection between the mode shapes at different axial stations, plane marching PSE [77] computations were performed across a range of disturbance frequencies and mode types, starting with the mode shapes at X locations that correspond to nearly neutral conditions. Unlike the PNP eigenvalue analysis, the PSE computations incorporate all of the important nonparallel effects on the disturbance evolution within the bulge. However, it is important to recall that the PSE ansatz constrains those computations to tracking a single disturbance with a unique local wavenumber in the marching direction. Because of the complex multimode topology of the unstable disturbances within the bulge region and the close proximity (and occasional crossings) of phase speeds between the different modes (see, for example, Fig. 6(b)), the accuracy of the PSE toward the prediction of the modal evolution becomes somewhat questionable. To help reduce that uncertainty, DNS computations were performed for a smaller group of frequencies and mode types that were selected on the basis of the amplification factors predicted by the PSE computations.

The disturbances in the DNS computations are introduced at the inflow boundary by using the mode shapes derived from the PSE computations for the appropriate modes. Similar to the PSE, the computational domain for DNS has a limited azimuthal extent; however, the DNS domain extends on both sides of the symmetry plane so that the symmetry characteristics of the disturbance field are determined by the inflow mode shape alone. The wall-normal extent of the computational domain extends well beyond the boundary-layer region. A typical DNS grid included 600 points across the streamwise domain and 301 points spanning the azimuthal extent of the computation. The wall-normal domain was resolved with 200 points, with clustering within the bulge region that is consistent with the expected mode shapes of the disturbance field. Additional simulations were performed in one case with finer grids in the streamwise and azimuthal directions. Given the focus of the DNS on validating the complex evolution of the disturbance field, the streamwise domain of the DNS extended from approximately $X \approx 0.20$ m, i.e., a short distance downstream of the range of neutral locations, up to nearly $X = 0.60$ m, i.e., well past the transition onset location measured in the experiment.

The PSE computations had shown that the most amplified disturbances in the bulge region have frequencies of around $f = 150$ kHz to $f = 200$ kHz. Therefore, separate DNS computations focused on the linear growth of symmetric and antisymmetric modes, respectively, across a frequency range of $f = 50$ kHz to $f = 300$ kHz. As discussed later in this section, the highest overall amplification within the bulge regions on both leeward and windward sides corresponds to an antisymmetric mode of instability. An illustrative comparison of the mode shape evolution for the dominant antisymmetric mode at $f = 200$ kHz is shown in Fig. 7, wherein the PSE predictions for the $|u'|$ mode shapes at selected streamwise locations are shown on the left in Fig. 7(a), whereas the results of DNS over a subset of the PSE domain are shown on the right in Fig. 7(b).

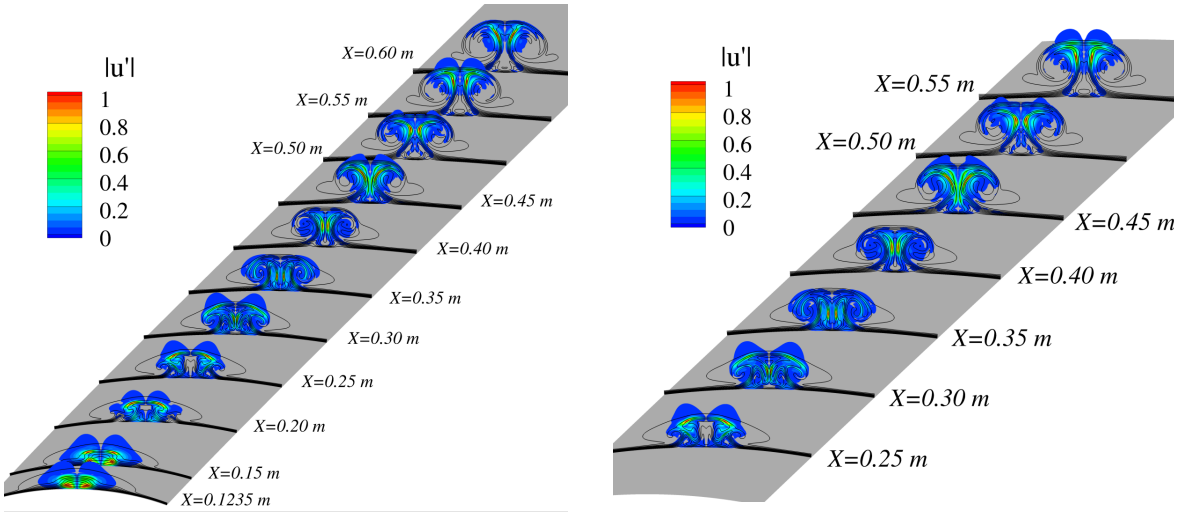

(a) Antisymmetric mode (PSE) (b) Antisymmetric mode (DNS)

Fig. 7. Mode shape evolution of the dominant antisymmetric instability mode at $f = 200$ kHz (leeward side).

Fig. 7(a) shows that the antisymmetric mode of interest has a single pair of peaks in the initial region of amplification (X = 0.1235 m) as against the dual peak structure of the most amplified Mack modes in Fig. 5(a). The single near wall peak is still suggestive of an oblique Mack mode disturbance. At X = 0.15 m, the shear layer bounding the mushroom shaped structure has already modified the original Mack mode structure to generate an additional pair of peaks near the spanwise ends of the shear layer along the cap of the bulge region. After that, the peak velocity fluctuations remain confined to that shear layer until X = 0.25 m. Between X = 0.30 m and X = 0.35 m, however, the peak shifts to a pair of vertical shear layers inside the stem region of the mushroom. Note that there is an additional pair of shear layers that bounds the stem region; however, those shear layers do not exhibit the dominant fluctuations. Across the entire downstream region until X = 0.6 m, the peak velocity fluctuations are located within the inner pair of shear layers within the stem region, with the peak location lifting up toward the corners between the stem region and the bottom of the mushroom cap. The mode shape evolution within the DNS solution in Fig. 7(b) indicates an identical trend to that in the PSE solution.

The axial evolution of the N-factor values (i.e., the logarithmic amplification ratios relative to the neutral station) for the antisymmetric modes at selected frequencies is plotted in Fig. 8, wherein the results based on both PSE and the DNS have been shown. The N-factor values are based on the peak $|u'|$ fluctuation across the cross section of the bulge region and the locations of rapid changes in the slopes of the N-factor curves correspond to the changes in the locations of peak velocity fluctuations as discussed in the preceding paragraph. Despite the fact that the N-factor curves based on the infinity norm of the $|u'|$ fluctuations present a stringent measure of comparison between the PSE predictions and the DNS, one observes an excellent agreement between the two sets of results, indicating the accuracy of the PSE to track the amplification of the bulge region instabilities over a 3D body surface.

Although not shown, additional DNS for the dominant symmetric modes across a range of disturbance frequencies from f = 50 kHz up to f = 300 kHz had indicated similarly excellent agreement with the N-factor predictions based on the PSE, confirming the accuracy of using the latter toward transition correlations in the present context. Finally, as discussed in regard to Fig. 6(b), the bulge region instabilities may propagate at supersonic phase speeds with respect to the local inviscid flow and that was also found to be true in the context of the spatial evolution of fixed frequency disturbances. The prevalence of supersonic speeds has not been emphasized in previous investigations of streak instabilities and this interesting feature should be investigated in greater detail during future work on the transition along the bulge region.

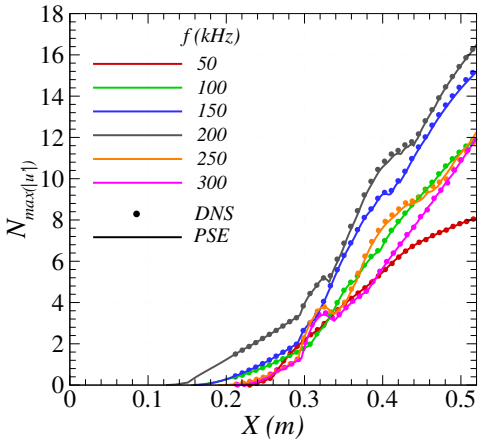

Fig. 8. Comparison of N-factor evolution for selected antisymmetric instability modes at different frequencies (leeward side). Lines correspond to the PSE predictions, whereas the DNS results are indicated via symbols of the same color.

Given the relatively modest angle of incidence, the mode shape evolution along the windward side of the model is qualitatively analogous to that over the leeward region, with the major difference between the leeward and windward sides being related to the azimuthal distance between the pair of streamwise vortices that comprise the bulge region. As a result, the basic state contours on the windward side indicate a highly distinct pair of bulges, one on each side of the plane of symmetry. Thus, the shear layer regions at the larger values of X appear as an approximately τ-shaped structure on the right half, combined with its mirror image in the left half of the cross section. As a result of these differences in the basic state structure, the stability analysis on the winward side also

uncovered certain new features of the instability modes that are discussed in the more comprehensive report based on the current investigation.

As described in Ref. [78], both the symmetric and the antisymmetric instability modes considered in the present study are able to achieve rather high values of logarithmic amplification ratio, i.e., the N-factor. However, the antisymmetric modes reach somewhat larger N-factor values near X = 0.5 m (corresponding to the approximate transition location inferred from inflight measurements along the leeward ray, as shown in Fig. 15 from Tufts et al. [52]), suggesting that the antisymmetric modes are more likely to induce transition at the selected time (barring, of course, any major differences in the receptivity and nonlinear stages associated with these modes). Figures 9(a) and 9(b) display the axial evolution of the N-factor associated with fixed-frequency disturbances of the antisymmetric disturbances on the windward and leeward sides, respectively. In general, the instability amplification begins near X = 0.2 m, and N-factors values of significantly greater than 10 are reached near X = 0.5 m. In agreement with the flight measurements, the results indicate a comparable but somewhat delayed disturbance amplification on the windward side. Although not shown herein, we note that the highest amplification ratio generally occurs not at the symmetry plane itself but at a pair of azimuthal locations on either side of the symmetry plane. This finding is qualitatively consistent with the surface flow visualizations from ground facility experiments see, for instance, Ref. [41]).

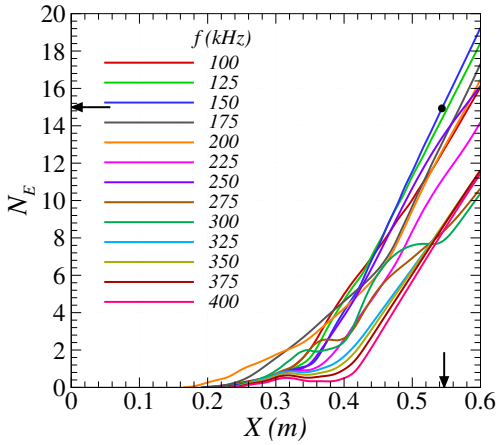

(b) Leeward side. The vertical arrow near X = 0.55 m denotes the location corresponding to the N-factor value based on part (b), as indicated by the horizontal arrow near N ≈ 15.

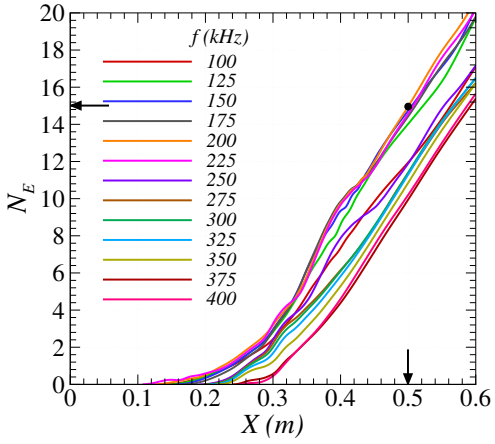

(b) Leeward side. The vertical arrow at X = 0.5 m denotes the transition location inferred from the flight data [52], whereas the horizontal arrow adjacent to the N_E axis denotes the peak N-factor at that location.

Fig. 9. Amplification characteristics of antisymmetric modes of instabilities within the bulge region. Each curve in these figures denotes the N-factor evolution of a fixed frequency disturbance from a given family of modes. .

Figure 9(b) indicates a peak N-factor value of approximately 15 at the estimated transition location along the leeward ray of the HIFiRE-5b test article [52]. However, the significant uncertainty in the transition location derived from the sparse array of instrumentation on the flight article may be expected to be accompanied by a comparable uncertainty in the N-factor correlation. In that regard, additional computations over a broader range of flight conditions should help provide a more robust value for the correlating N-factor. The rapid rise in the N-factor envelope as a function of X implies that the sensitivity of predicted transition location to the chosen value of the correlating N-factor would be relatively modest, with $\Delta(X/L)/\Delta N \approx 2\%$ in Fig. 9(b). Because of the similarity between the bulge region instabilities at upstream stations and the frequently encountered class of Mack mode instabilities, it is worthwhile to see how the above N-factor compares with the N-factor correlation for Mack mode transition during the HIFiRE-1 flight experiment. For the HIFiRE-1 experiment with a circular cone at nearly zero degrees angle of attack, Li et al. [20] quote an N-factor correlation of 13.4 for Mack mode transition, on the basis of averaging the N-factor values at five separate trajectory points from the (Table 3 from Ref. [20]). However, if one ignores the earliest data point (t = 19 s) from their results as an outlier by virtue of its proximity in time to the bypass transition at earlier times, then the correlated N-factor averaged between the time instances of t = 20, 21, and 22 s

becomes equal to 13.9, which is close to the abovementioned N-factor for bulge region instabilities in the present case. Thus, it appears that, regardless of which of the two N-factor correlations based on the HIFiRE-1 flight data is used, applying the HIFiRE-1criterion to the present case would have resulted in reasonable estimates of transition along the centerline. On the other hand, it should also be noted that the analysis by Tufts et al. [52] for the HIFiRE-5b flight configuration had indicated a preliminary N-Factor threshold of N = 18 for second mode transition along the attachment line of the HIFiRE-5b test article and N = 10 for the transition due to stationary crossflow instabilities over much of the acreage.

IV. Conclusions

This paper has extended the previous analyses of the HIFiRE-5b flight experiment by addressing the linear stability characteristics of the boundary layer flow within the bulge region near the planes of symmetry along the minor axes of the elliptic cone. At the trajectory point corresponding to t = 514.83 seconds, the frequencies of the amplified disturbances are in the range of hundreds of kHz, with the most amplified instability modes near X = 0.5 m being in the range of approximately 150-225 kHz. An excellent agreement is found between the predictions of the plane marching PSE and the DNS results, demonstrating that the PSE can provide an efficient and accurate technique to predict the disturbance growth in hypersonic boundary layers with streak-like flow features that support multiple locally unstable modes. The present results also serve as an extension of similar comparisons from the earlier work on the amplification of secondary instabilities of stationary crossflow vortex patterns over a yawed circular cone to the fully 3D geometry of an elliptic cone. An additional noteworthy finding pertains to the locally supersonic phase speeds of the bulge region instabilities over significant distances preceding the onset of transition. Furthermore, the linear stability analysis yields a peak N-factor of approximately 15 at the transition location estimated from the flight data along the leeward ray, which happens to be close to the N-factor value that correlates with Mack mode transition during the HIFiRE-1 circular cone experiment at zero degrees angle of attack.

The analysis described in the present paper thus provides the foundation for a more comprehensive analysis toward the development of a N-factor correlation for the bulge region transition via similar analysis for a broader set of trajectory locations from the HIFiRE-5b flight experient. The results of such analysis will be reported in a future paper.

Acknowledgments

This work was performed as part of the Hypersonic Technology Project and Revolutionary Computational Aerosciences discipline under the Transformational Tools and Technologies project of the NASA Transformative Aeronautics Concepts Program. Computational resources for this work were provided by the NASA High-End Computing (HEC) Program through the NASA Advanced Supercomputing (NAS) Division at Ames Research Center. The authors would like to acknowledge useful technical communications with Dr. Matthew Tufts from the Air Force Research Laboratory and Prof. Thomas Juliano from the University of Notre Dame.

References

[1] Stetson, K. F., Thompson, E. R., Donaldson, J. C., and Siler, L. G., "Laminar Boundary Layer Stability Experiments on a Cone at Mach 8 – Part 3: Sharp Cone at Angle of Attack," AIAA Paper 85-0492, 1985.

[2] Schneider, S. P., "Hypersonic Laminar-Turbulent Transition on Circular Cones and Scramjet Forebodies," *Progress in Aerospace Sciences*, Vol. 40, 2004, pp. 1–5.

[3] Swanson, E. and Schneider, S. P., "Boundary-Layer Transition on Cones at Angle of Attack in a Mach-6 Quiet Tunnel," AIAA Paper 2010-1062, 2010.

[4] Li, F., Choudhari, M., Chang, C.-L., and White, J., "Analysis of Instabilities in Non-Axisymmetric Hypersonic Boundary Layers over Cones," AIAA Paper 2010-4643, 2010.

[5] Balakumar, P. and Owens, L., "Stability of Hypersonic Boundary Layers on a Cone at Angle of Attack," AIAA Paper 2010-4718, 2010.

[6] Munoz, F., Heitmann, D., and Radespiel, R., "Instability Modes in Boundary Layers of an Inclined Cone at Mach 6," *Journal of Spacecraft and Rockets*, Vol. 51, No. 2, 2014, pp. 442–454.

[7] Ward, C. A. C., Henderson, R. O., and Schneider, S. P., "Possible Secondary Instability of Stationary Crossflow Vortices on an Inclined Cone at Mach 6," AIAA Paper 2015-2773, 2015.

[8] Li, F., Choudhari, M., Paredes, P., and Duan, L., "Secondary Instability of Stationary Crossflow Vortices in Mach 6 Boundary Layer over a Circular Cone," NASA/TM-2015-218997, Dec. 2015.

[9] Poggie, J. and Kimmel, R., "Traveling Instability Waves in a Mach 8 Flow over an Elliptic Cone," *AIAA Journal*, Vol. 38, No. 2, 2000, pp. 251–258.

[10] Kimmel, R. L., Poggie, J. and Schwoerke, S. N., "Laminar-Turbulent Transition in a Mach 8 Elliptic Cone Flow," *AIAA Journal*, Vol. 37, No. 9, 1999, pp. 1080–1087.
[11] Holden, M., "Experimental Studies of Laminar, Transitional, and Turbulent Hypersonic Flows Over Elliptic Cones at Angle of Attack," Air Force Office of Scientific Research Technical Report AFRL-SR-BL-TR-98-0142, Bolling Air Force Base, DC, 1998.
[12] Choudhari, M., Chang, C.-L., Li, F., Berger, K., Candler, G., and Kimmel, R., "Transition Analysis for the HIFiRE-5 Vehicle," AIAA Paper 2009-4056, 2009.
[13] Li, F., Choudhari M., Chang, C.-L., White, J. A., Kimmel, R., Adamczac, D., Borg, M., Stanfeld, S., and Smith, M., "Stability Analysis for HIFiRE Experiments," AIAA Paper 2012-2961, 2012.
[14] Juliano, T., Borg, M., and Schneider, S. P., "Quiet Tunnel Measurements of HIFiRE-5 Boundary-Layer Transition," *AIAA Journal*, Vol. 53, 2015, pp. 832–84.
[15] Borg, M., Kimmel, R. A., and Stanfield, S., "Traveling Crossflow Instability for the HIFiRE-5 Elliptic Cone," *Journal of Spacecraft and Rockets*, Vol. 52, 2015, pp. 664–673.
[16] Paredes, P., Gosse, R., Theofilis, V., and Kimmel, R. L., "Linear Modal Instabilities of Hypersonic Flow over an Elliptic Cone," *J. Fluid Mechanics*, Vol. 804, 2016, pp. 442–466.
[17] Dolvin, D. J., "Hypersonic International Flight Research and Experimentation Technology Development and Flight Certification Strategy," AIAA Paper 2009-7228, October 2009.
[18] Kimmel, R. L., Adamczak, D., Paull, A., Paull, R., Shannon, J., Pietsch, R., Frost, M., and Alesi, H., "HIFiRE-1 Ascent-Phase Boundary-Layer Transition," *Journal of Spacecraft and Rockets*, Vol. 52, No. 1, 2015, pp 217-230.
[19] Stanfield, S. A., Kimmel, R. L., Adamczak, D. and Juliano, T. J., "HIFiRE-1 Data Analysis: Boundary Layer Transition Experiment During Reentry," *Journal of Spacecraft and Rockets*, Vol. 52, No. 3, 2015, pp 637-649.
[20] Li, F., Choudhari, M., Chang, C.-L., Kimmel, R., Adamczak, D., and Smith, M., "Transition Analysis for the Ascent Phase of HIFiRE-1 Flight Experiment," *Journal of Spacecraft and Rockets*, Vol. 52, No. 5, 2015, pp. 1283-1293.
[21] Kimmel, R. L., Adamczak, D. A., and DSTG AVD Brisbane Team, "HIFiRE-5b Flight Overview," AIAA Paper 2017-3131, June 2017.
[22] Kimmel, R. L., Adamczak, D., Hartley, D., Alesi, H., Frost, M., Pietsch, R., Shannon, J., and Sylvester, T., "Hypersonic International Flight Research Experimentation-5b Flight Overview," Paper 2017-3131, 2017.
[23] Tufts, M. P., Borg, M., Gosse, R., and Kimmel, R. L., "Collaboration Between Flight Test, Ground Test, and Computation on HIFiRE-5," AIAA Paper 2018-3807, 2018.
[24] Paredes, P. and Theofilis, V., "Centerline Instabilities on the Hypersonic International Flight Research Experimentation HIFiRE-5 Elliptic Cone Model," *Journal of Fluids and Structures*, Vol. 53, 2015, pp. 36–49.
[25] Berger, K. T., Rufer, S. J., Kimmel, R. L., and Adamczak, D., "Aerothermodynamic Characteristics of Boundary Layer Transition and Trip Effectiveness of the HIFiRE Flight 5 Vehicle," AIAA Paper 2009-4055, 2009.
[26] Holden, M. S., Wadhams, T. P., MacLean, M., and Mundy, E., "Review of Studies of Boundary Layer Transition in Hypersonic Flows Over Axisymmetric and Elliptic Cones Conducted in the CUBRC Shock Tunnels," AIAA Paper 2009-0782, 2009.
[27] Juliano, T. J., Schneider, S., "Instability and Transition on the HIFiRE-5 in a Mach 6 Quiet Tunnel," AIAA paper 2010-5004, June 2010.
[28] Borg, M., Kimmel, R. L., and Stanfield, S., "Instability and Transition for HIFiRE-5 in a Hypersonic Quiet Wind Tunnel," AIAA Paper 2011-3247, June 2011.
[29] Holden, M. S., Wadhams, T. P., MacLean, M., Dufrene, A., Mundy, E. and Marineau, E., "A Review of Basic Research and Developmen Programs Conducted in the LENS Facilities in Hypervelocity Flows," AIAA Paper 2012-0469, 2012.
[30] Borg, M. P., Kimmel, R. L., Stanfield, S., "Crossflow Instability for HIFiRE-5 in a Quiet Hypersonic Wind Tunnel," AIAA Paper 2012-2821, June 2012.
[31] Borg, M. P., Kimmel, R. L., and Stanfield, S., "Traveling Crossflow Instability for HIFiRE-5 in a Quiet Hypersonic Wind Tunnel," AIAA 2013-2737, June 2013.
[32] Borg, M. P., Kimmel, R. L., Hofferth, J. W., Bowersox, R. D., and Mai, C. L., "Freestream Effects on Boundary Layer Disturbances for HIFiRE-5," Paper 2015-0278, AIAA, January 2015.
[33] Borg, M. P., and Kimmel, R. L., "Traveling Crossflow Instability for the HIFiRE-5 Elliptic Cone," *Journal of Spacecraft and Rockets*, Vol. 52, No. 3, 2015, pp. 664-673.
[34] Borg, M. P., Kimmel, R. L., Hofferth, J. W., Bowersox, R. D., and Mai, C. L., "Freestream Effects on Boundary Layer Disturbances for HIFiRE-5," AIAA Paper 2015-0278, 2015.
[35] Juliano, T. J., Borg, M. P., and Schneider, S. P., "Quiet Tunnel Measurements of HIFiRE-5 Boundary-Layer Transition, *AIAA Journal*, Vol. 53, No. 4, 2015, pp. 832-846.
[36] Borg, M. P. and Kimmel, R. L., "Simultaneous Infrared and Pressure Measurements of Crossflow Instability Modes for HIFiRE-5," AIAA Paper 2016-0354, 2016.
[37] Neel, I. T., Leidy, A., and Bowersox, R. D., "Preliminary Study of the Eect of Environmental Disturbances on Hypersonic Crossfow Instability on the HIFiRE-5 Elliptic Cone," AIAA Paper 2017-0767, 2017.
[38] Juliano, T. J., Poggie, J., Porter, K. M., Kimmel, R. L., Jewell, J. S., and Adamczak, D. W., "HIFiRE-5b Heat Flux and Boundary-Layer Transition," AIAA Paper 2017-3134, 2017.
[39] Juliano, T. J., Poggie, J., Porter, K. M., Kimmel, R. L., Jewell, J. S., and Adamczak, D. W., "HIFiRE-5b Heat Flux and Boundary-Layer Transition," *Journal of Spacecraft and Rockets*, Vol. 55, No. 6, Nov. Dec. 2018, pp. 1315–1328.

[40] Neel, I. T., Leidy, A., Tichenor, N. R., and Bowersox, R. D., "Influence of Environmental Disturbances on Hypersonic Crossflow Instability on the HIFiRE-5 Elliptic Cone," AIAA Paper 2018-1821, 2018.
[41] Neel, I. T., Leidy, A., Tichenor, N. R., and Bowersox, R. D., "Characterization of Environmental Disturbances on Hypersonic Crossflow Instability on the HIFiRE-5 Elliptic Cone," AIAA Paper 2018-5375, 2018.
[42] Kimmel, R. L., Adamczak, D. W., Hartley, D., Alesi, H., Frost, M. A., Pietsch, R., Shannon, J., and Silvester, T., "Hypersonic International Flight Research Experimentation-5b Flight Overview," *Journal of Spacecraft and Rockets*, Vol. 55, No. 6, 2018, pp. 1303–1314.
[43] Jewell, J. S., Kimmel, R. L., Adamczak,D.W., Poggie, J., Porter,K. M., and Juliano, T. J., "HIFiRE-5b Flow Computations and Attitude Determination via Comparison with Flight Data," *Journal of Spacecraft and Rockets*, Vol. 55, No. 6, Nov.–Dec. 2018, pp. 1356–1368.
[44] Kimmel, R. L., Adamczak, D. W., Borg, M. P., Jewell, J. S., Juliano, T. J., Stanfield, S., and Berger, K. T., "HIFiRE-1 and -5 Flight and Ground Tests," AIAA Paper 2018-0056, 2018.
[45] Borg, M. P. and Kimmel, R. L., "Ground Test of Transition for HIFiRE-5b at Flight-Relevant Attitudes," *Journal of Spacecraft and Rockets*, Vol. 55, No. 6, 2018, pp. 1329-1340.
[46] Kimmel, R. L., Adamczak, D. W., Hartley, D., Alesi, H., Frost, M. A., Pietsch, R., Shannon, J., and Silvester, T., "Hypersonic International Flight Research Experimentation-5b Flight Overview," *Journal of Spacecraft and Rockets*, Vol. 55, No. 6, 2018, pp. 1303-1314.
[47] Jewell, J. S., Kimmel, R. L., Adamczak, D. W., Poggie, J., Porter, K. M., Juliano, T. J., "HIFiRE-5b Flow Computations and Attitude Determination via Comparison with Flight Data," *Journal of Spacecraft and Rockets*, Vol. 55, No. 6, 2018, pp. 1356-1368.
[48] Juliano, T. J., Jewell, J. S., and Kimmel, R. L., "Effects of Attitude on HIFiRE-5b Boundary-Layer Transition," *J. Spacecraft and Rockets.*, Vol. 56, No. 4, 2019, pp. 1045–1059.
[49] Juliano, T. J., Paquin, L. A., and Borg, M. P., "HIFiRE-5 Boundary-Layer Transition Measured in a Mach-6 Quiet Tunnel with Infrared Thermography," *AIAA Journal*, Vol. 57, No. 5, 2019, pp. 2001-2010.
[50] Juliano, T. J., Jewell, J. S., and Kimmel, R. L. "HIFiRE-5b Boundary-Layer Transition Length and Turbulent Overshoot," AIAA Paper 2019-2970, 2019.
[51] Li, F., Choudhari, M., Chang, C.-L., White, J., Kimmel, R., Adamczak, D., Borg, M., Stanfield, S., and Smith, M., "Stability Analysis for HIFiRE Experiments," AIAA paper 2012-2961, June 2012.
[52] Tufts, M. P., Gosse, R., and Kimmel, R. L., "PSE Analysis of Crossflow Instability on HIFiRE 5b Flight Test," AIAA Paper 2017-0764, January 2017.
[53] Moyes, A. J., Paredes, P., Kocian T. S., and Reed, H., "Secondary Instability Analysis of Crossflow on a Hypersonic Yawed Straight Circular Cylinder," AIAA Paper 2016-0848, 2016.
[54] Tokugawa, N., Choudhari, M., Ishikawa, H., Ueda, Y., Fujii, K., Atobe, T., Li, F., Chang, C.-L., and White, J., "Transition Along Leeward Ray of Axisymmetric Bodies at Incidence in Supersonic Flow," *AIAA Journal*, Vol. 53, No. 12, 2015, pp. 3737–3751. doi: 10.2514/1.J054070
[55] Choudhari, M., Tokugawa, N., Li, F., Chang, C.-L., White, J., Ishikawa, H., Ueda, Y., Atobe, T., and Fujii, K., "Computational Investigation of Supersonic Boundary Layer Transition over Canonical Fuselage Nose Configurations," Proc. of 7th Intl. Conference on Computational Fluid Dynamics, Island of Hawaii, June 2012. (http://www.iccfd.org/iccfd7/assets/pdf/papers/ICCFD7-2306_paper.pdf)
[56] Li, F., Choudhari, M., Paredes, P., and Duan, L., "Secondary Instability of Stationary Crossflow Vortices in Mach 6 Boundary Layer over a Circular Cone," NASA/TM-2015-218997, Dec. 2015.
[57] Li, F., Choudhari, M., Paredes, P., and Duan, L., "High-Frequency Instabilities of Stationary Crossflow Vortices in a Hypersonic Boundary Layer," *Phys. Rev. Fluids*, Vol. 1, 2016, 053603.
[58] Choudhari, M., Li, F., Paredes, P., and Duan, L., "Computations of Crossflow Instability in Hypersonic Boundary Layers," AIAA Paper 2017-4300, 2017.
[59] Choudhari, M., Paredes, P., and Duan, L., "Nonlinear Evolution and Breakdown of Azimuthally Compact Crossflow Vortex Pattern over a Yawed Cone," AIAA Paper 2018-1823, 2018.
[60] Li, F., Choudhari, M. M., Paredes, P., Schneider, S. P. and Portoni, P., "Görtler Instability and Its Control via Surface Suction Over an Axisymmetric Cone at Mach 6," AIAA paper 2018-3069.
[61] Li, F., Choudhari, M. M., and Paredes, P., "Nonlinear Görtler Vortices and Their Secondary Instability in a Hypersonic Boundary Layer," AIAA paper 2019-3216, 2019.
[62] Choudhari, M., Li, F., Parades, P., and Duan, L., "Effect of 3D Roughness Patch on Instability Amplification in a Supersonic Boundary Layer," AIAA Paper 2019-0877, 2019.
[63] Paredes, P., Choudhari, M., and Li, F., "Laminar-Turbulent Transition Upstream of the Entropy-Layer Swallowing Location in Hypersonic Boundary Layers," AIAA Paper 2019-3215, 2019.
[64] vulcan-cfd.larc.nasa.gov (last accessed October 17, 2016)
[65] van Albada, G. D., van Leer, B., and Roberts, W. W., "A Comparative Study of Computational Methods in Cosmic Gas Dynamics," *Astronomy and Astrophysics*, Vol. 108, 1982, pp. 76–84.
[66] Edwards, J. R., "A Low-Diffusion Flux-Splitting Scheme for Navier-Stokes Calculations," *Computers and Fluids*, Vol. 6, 1997, pp. 635–659.
[67] Litton, D., Edwards, J., and White, J., "Algorithmic Enhancements to the VULCAN Navier-Stokes Solver," AIAA Paper 2003-3979, 2003.

[68] Cheatwood, F. M. and Gnoffo, P. A., "User's Manual for the Langley Aerothermodynamic Upwind Relaxation Algorithm (LAURA)," NASA TP 4674, April 1996.
[69] Wu, M. and Martin, M. P., "Direct Numerical Simulation of Supersonic Boundary Layer over a Compression Ramp," *AIAA Journal*, Vol. 45, No. 4, 2007, pp. 879–889.
[70] Jiang, G. S. and Shu, C. W., "Efficient Implementation of Weighted ENO Schemes," *J. Comp. Phys.*, Vol. 126, No. 1, 1996, pp. 202–228.
[71] Taylor, E. M., Wu, M., and Martin, M. P., "Optimization of Nonlinear Error Sources for Weighted Non-Oscillatory Methods in Direct Numerical Simulations of Compressible Turbulence," *J. Comp. Phys.*, Vol. 223, No. 1, 2006, pp. 384–397.
[72] Williamson, J., "Low-Storage Runge-Kutta Schemes," *J. Comp. Phys.*, Vol. 35, No. 1, 1980, pp. 48–56.
[73] Duan, L., Beekman, I., and Martin, M. P., "Direct Numerical Simulation of Hypersonic Turbulent Boundary Layers. Part 3: Effect of Mach Number," *J. Fluid. Mech.*, Vol. 672, 2011, pp. 245–267.
[74] Duan, L., Choudhari, M., and Li, F., "Direct Numerical Simulation of Crossflow-Induced Transition in a Swept Wing Boundary Layer," AIAA Paper 2013-2617, 2013.
[75] Choudhari, M., Li, F., Duan, L., Carpenter, M. H., Streett, C. L., and Malik, M. R., "Towards Bridging the Gaps in Holistic Transition Prediction via Numerical Simulations," AIAA Paper 2013-2718, 2013.
[76] Choudhari, M., Li, F., Chang, C., Norris, A., and Edwards, J., "Wake Instabilities behind Discrete Roughness Elements in High Speed Boundary Layers," AIAA Paper 2013-81, 2013.
[77] Paredes, P., Hanifi, A., Theofilis, V., and Henningson, D., "The Nonlinear PSE-3D Concept for Transition Prediction in Flows with a Single Slowly-Varying Spatial Direction," Procedia IUTAM, Vol. 14C, 2015, pp. 35-44.
[78] Choudhari, M., Li, F., and Paredes, P., "Centerline Transition Over an Elliptic Cone at Flight Conditions," To be submitted for publication.